PAPER • OPEN ACCESS

Attosecond streaking metrology with isolated nanotargets

View the article online for updates and enhancements.

Related content

- Attosecond physics at the nanoscale
  M F Ciappina, J A Pérez-Hernández, A S Landsman et al.

- Advances in attosecond science
  Francesca Calegari, Giuseppe Sansone, Salvatore Stagira et al.

- Carrier–envelope phase-tagged imaging of the controlled electron acceleration from SiO2 nanospheres in intense few-cycle laser fields
  S Zherebtsov, F Süßmann, C Peltz et al.

Recent citations

- All-optical spatio-temporal control of electron emission from SiO_2 nanospheres with femtosecond two-color laser fields
  Qingcao Liu *et al*

- Emerging attosecond technologies
  Johan Mauritsson *et al*

IOP ebooks™

Bringing you innovative digital publishing with leading voices to create your essential collection of books in STEM research.

Start exploring the collection - download the first chapter of every title for free.

Attosecond streaking metrology with isolated nanotargets

Q Liu[1,2], L Seiffert[3] , A Trabattoni[4], M C Castrovilli[5], M Galli[5,6], P Rupp[1,2],
F Frassetto[7], L Poletto[7], M Nisoli[6], E Rühl[8], F Krausz[1,2], T Fennel[3,9] ,
S Zherebtsov[1,2], F Calegari[4,5,10] and M F Kling[1,2,10]

[1] Max Planck Institute of Quantum Optics, Hans-Kopfermann-Str. 1, D-85748 Garching, Germany
[2] Department of Physics, Ludwig-Maximilians-Universität München, Am Coulombwall 1, D-85748 Garching, Germany
[3] Institute of Physics, University of Rostock, Albert-Einstein-Str. 23, D-18059 Rostock, Germany
[4] Center for Free-Electron Laser Science, DESY, Notkestr. 85, D-22607 Hamburg, Germany
[5] National Research Council of Italy, Institute for Photonics and Nanotechnologies, Piazza L. Da Vinci 32, I-20133 Milano, Italy
[6] Department of Physics, Politecnico di Milano, Piazza L. Da Vinci 32, I-20133 Milano, Italy
[7] National Research Council of Italy, Institute for Photonics and Nanotechnologies, Via Trasea 7, I-35131 Padova, Italy
[8] Physical Chemistry, Freie Universität Berlin, Takustr. 3, D-14195 Berlin, Germany
[9] Max Born Institute, Max-Born-Straße 2A, D-12489 Berlin, Germany

E-mail: francesca.calegari@desy.de and matthias.kling@lmu.de

CrossMark

Abstract

The development of attosecond metrology has enabled time-resolved studies on atoms, molecules, and (nanostructured) solids. Despite a wealth of theoretical work, attosecond experiments on isolated nanotargets, such as nanoparticles, clusters, and droplets have been lacking. Only recently, attosecond streaking metrology could be extended to isolated silica nanospheres, enabling real-time measurements of the inelastic scattering time in dielectric materials. Here, we revisit these experiments and describe the single-shot analysis of velocity-map images, which permits to evaluate the recorded number of electrons. Modeling of the recorded electron histograms allows deriving the irradiated nanoparticle statistics. Theoretically, we analyze the influence of the nanoparticle size on the field-induced delay, which is one of the terms contributing to the measured streaking delay. The obtained new insight into attosecond streaking experiments on nanoparticles is expected to guide wider implementation of the approach on other types of nanoparticles, clusters, and droplets.

(Some figures may appear in colour only in the online journal)

---

[10] Authors to whom any correspondence should be addressed.

1. Introduction

Recent advances in laser technology and ultrashort pulse generation have permitted to record electron dynamics on timescales reaching into the attosecond domain [1, 2]. Since the advent of attosecond physics [3, 4], the field has come very far and several metrologies for the real-time observation of electron dynamics have been developed and demonstrated

Figure 1. Attosecond interferometer used for streaking measurements. Polarization gating (PG) optics were used to properly manipulate the polarization of the driving pulse. Fused silica (FS) wedges in both arms permitted to adjust the dispersion and the CEP of the NIR pulses.

(for an overview see e.g. [5–8]). Among the most commonly used techniques is attosecond streaking spectroscopy [9–11]. Here, the photoemission of electrons is typically initiated by an attosecond extreme ultraviolet (XUV) pulse, and the momentum change of released electrons due to a second, intense near-infrared (NIR) pulse is measured as a function of XUV/NIR pulse delay. Attosecond streaking spectroscopy has been applied in studies on atoms [2, 12–15], metals [16–21] or adlayer-covered metals [22, 23], providing insight into photoemission delay, electron correlation, propagation and scattering, and screening.

Attosecond streaking spectroscopy has also been suggested as a suitable metrology for measuring collective electron dynamics in nanostructures [24–30]. The spatial homogeneity of the driving laser field is one of the key aspects in attosecond streaking of atoms [2, 13, 15]. Nanosystems, in contrast, exhibit spatially inhomogeneous nearfields, which strongly vary in amplitude and phase from the exciting laser field. The local fields can be enhanced by orders of magnitude and their spatial properties generally depend on material properties, shape, and environment [31, 32].

The application of attosecond streaking spectroscopy to nanosystems was introduced by Stockman *et al* [24] for metallic nanostructures, where localized or propagating surface plasmons can be excited, exhibiting such large local oscillator strength that they can dominate the acceleration of released electrons. In these cases, the energy of the external, exciting laser field can be localized to nanometer scales, below the diffraction limit of the exciting light [33]. Since the first theoretical proposal in 2007 [24], much progress has been made in measuring the near-field driven photoemission from metallic nanotips with streaking spectroscopy on femtosecond [34, 35] and attosecond timescales [36, 37], and in advancing attosecond photoemission electron microscopy [38–40]. Despite this progress and a wealth of theoretical studies [25, 27–30], the translation of attosecond streaking spectroscopy to isolated nanoparticles has posed a formidable challenge. Only very recently, the first experiment has been successfully implemented [41].

In the proof-of-principle experiment [41], the delayed photoemission from dielectric nanoparticles was measured and served as a stopwatch for electron scattering. It is noteworthy that such measurements could not be implemented on stationary dielectric solids owing to the accumulative charging from the XUV-driven electron emission. In the experiments on nanoparticles, a continuous stream of aerosolized nanospheres circumvented this problem, enabling the chronoscopy of inelastic scattering in dielectrics [41].

Here, we detail the conditions and technological advances that have enabled the implementation of attosecond streaking spectroscopy on isolated nanoparticles. We extend the analysis of the data shown in [41] to obtain single-shot electron statistics, which in turn provides information on the laser-irradiated particle statistics within the laser interaction. Furthermore, we extend our modeling of the field-induced delay contribution to the measured streaking delay as a function of nanoparticle size. The new information paves the way towards related experiments on other material classes and other nanoscopic targets such as clusters and droplets.

2. Experimental approach

2.1. Attosecond setup

The attosecond setup is especially designed to achieve sufficiently high photon flux to perform time-resolved spectroscopy of low-density targets such as isolated nanoparticles. The setup is driven by NIR, sub 4 fs, 2.5 mJ pulses obtained by hollow-core fiber compression of 25 fs, 6 mJ, 780 nm pulses from a commercial Ti:sapphire laser system (Femtopower V Pro CEP, Spectra-Physics). To achieve maximum coupling efficiency, the hollow-core fiber compressor is operated in pressure-gradient configuration. The residual single-shot carrier-envelope phase (CEP) fluctuation of the driving pulses is ~200 mrad (rms) [42]. A schematic of the attosecond setup is shown is figure 1. A portion of the NIR beam (70%) is focused by a 1 m radius-of-curvature spherical mirror into a static gas cell filled with a noble gas to produce XUV radiation by high-order harmonic generation. A continuous emission spectrum corresponding to isolated attosecond pulses is achieved with the polarization gating technique [43]. A pair of fused silica wedges is used to properly adjust dispersion and CEP of the NIR driving pulses. The fundamental radiation and
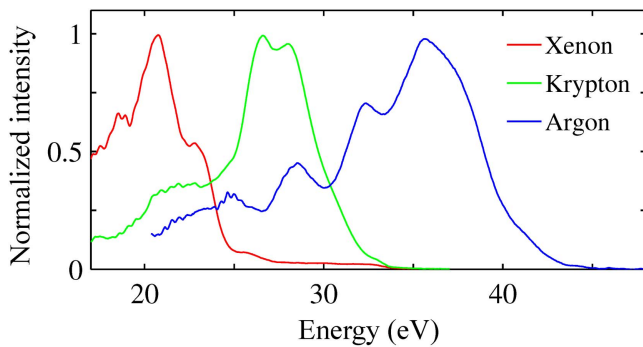
Figure 2. Continuous XUV spectra generated in xenon (red curve), krypton (green curve) and argon (blue curve). The spectra have been acquired by using a high-resolution flat-field soft x-ray spectrometer. Full tunability between 16 and 45 eV is achieved.

the energy region of the spectrum below 16 eV are filtered out by a 100 nm thick aluminum filter. The remaining portion of the NIR beam (30%) is properly delayed with attosecond resolution by using a piezo-stage and then collinearly recombined with the XUV beam by using a drilled mirror with a 3 mm diameter central hole in an interferometric configuration. The interferometer is actively stabilized using a frequency stabilized He–Ne laser.

In a typical time-resolved measurement, the pulse delay (Δt) therefore measures the delay of the NIR pulse with respect to the XUV pulse. An additional pair of fused silica wedges is used to properly adjust dispersion and CEP of the NIR probe pulses. A gold-coated toroidal mirror ($f = 90$ cm) is used to focus both the XUV and NIR pulses into a beam of nanoparticles and the resulting electron photoemission is detected with a single-shot velocity-map imaging (VMI) spectrometer (see section 2.2) [44, 45]. The toroidal mirror is operated in Rowland configuration with unity magnification and provides an almost aberration-free image of the XUV source, with a negligible temporal smearing of the attosecond pulses. The spectral characterization of the XUV radiation is simultaneously achieved by using a high-resolution flat-field soft x-ray spectrometer consisting of a second gold-coated toroidal mirror, followed by a grating, a microchannel plate (MCP), a phosphor screen, and a charge-coupled device camera [46]. The angle of incidence of the toroidal mirror is 86° and two gratings (Hitachi 001-0639 and 001-0640) are used to cover the energy range 12–100 eV. As can be seen from figure 2, completely tunable XUV emission covering the energy region between 16 and 45 eV can be achieved by using different generation gases (xenon, krypton or argon). The XUV photon flux has been measured on target by using a National Institute of Standard and Technology calibrated open photo-diode. The current from the photodiode, proportional to the number of incidence photons, is read by a Keithley amperemeter. When generating XUV pulses in xenon, their energy in the case of continuous spectra is ∼4 nJ, measured after the 100 nm thick aluminium filter. Such an energy corresponds to ∼8 × 10^8 photons/pulse (or ∼8 × 10^{11} photons s^{-1} for a repetition rate of 1 kHz of the laser system).

To temporally characterize the XUV and NIR pulses, the attosecond beamline is also equipped with a time-of-flight spectrometer to perform attosecond streaking in argon gas. For reconstruction of the laser fields, the frequency-resolved-optical-gating for complete-reconstruction-of-attosecond-bursts (FROG-CRAB) technique is used [47]. Measured and reconstructed streaking traces are presented in figures 3(a) and (b), respectively. The retrieved temporal intensity profile and phase of the XUV pulses are shown in figure 3(c). A pulse duration of 250 as is typically achieved using the described setup.

2.2. Single-shot VMI

The setup for single-shot attosecond VMI with nanoparticles is schematically shown in figure 4. The delay-controlled XUV and NIR pulses propagate collinearly in positive direction along the *x*-axis, and are polarized along the *y*-axis. The nanoparticle stream is injected into the interaction region by an aerodynamic lens along the *y*-axis. The homogeneous static electric fields between the electrodes accelerate photo-electrons towards the MCP/phosphor screen detector with an active diameter of 80 mm (F2226-24PX, Hamamatsu). The supply voltages of the detector were gated by a fast high-voltage switch with a gate width of 300 ns (HTS-41-03 GSM, Behlke) to reduce background contributions. The VMI on the phosphor screen were recorded by a high-speed digital complementary metal-oxide-semiconductor (CMOS) camera. The camera was operated at the laser repetition rate (1 kHz) with a resolution of 800 × 600 pixels, and the exposure time was 0.1 ms. For each image, the camera software (Marathon Pro, GS Vitec) applied a flat-field correction, and up to 1024 pixels with a brightness above a defined threshold were recorded (see [48] for details). This approach significantly reduced the amount of data and enabled storage of single-shot images at the full repetition rate. The camera and the fast high voltage switch are both synchronized to the laser with suitably delayed TTL-trigger signals.

2.3. Aerosol generation

In the studies described here, the aerosol generation system consisted of an evaporator, silica drying stage, impactor, pressure equalizer (figure 5), and the aerodynamic lens with subsequent differential pumping. The aerosol is evaporated from a nanoparticle suspension by a commercial aerosol generator (model 3076, TSI). The carrier gas is neon, and the evaporation pressure is 1.75 bar. The nanoparticle density in the aerosol is determined by the nanoparticle concentration in the suspension and the evaporation gas pressure. The aerosol is sent through the diffusion dryer (model 3062, TSI) to remove residual solvent from the aerosol. The impactor consists of a sharp 90° turn, and blocks nanoparticle clusters. A pressure equalizer (HEPA Capsule Filter 1602051, TSI) is installed in front of the aerodynamic lens system to level the input pressure to one atmosphere.

An aerodynamic lens system typically consists of a flow control orifice, a series of focusing lenses and an acceleration
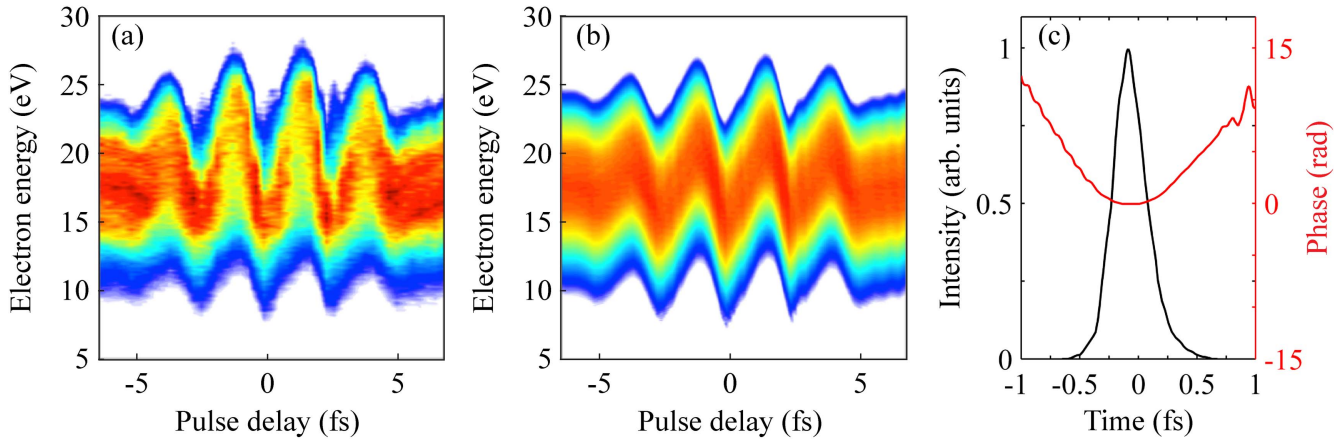
Figure 3. Attosecond pulse characterization. (a) Attosecond streaking spectrogram measured in argon and (b) retrieved FROG-CRAB trace. (c) Reconstructed temporal intensity profile of the XUV pulse. The retrieved pulse duration was 250 ± 20 as full-width-at-half-maximum with a residual parabolic phase indicating the presence of small second-order dispersion. The second-order dispersion value was determined *in situ* in the main experiments from residual gas data.
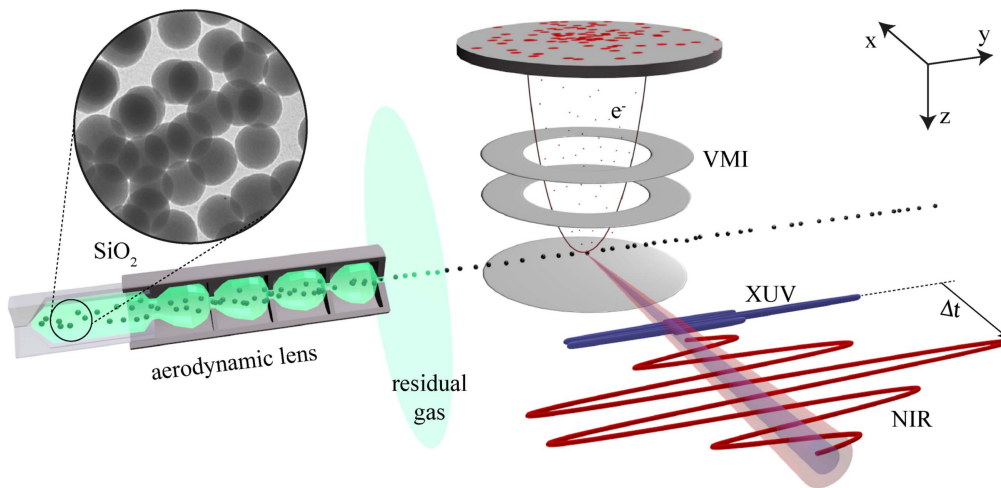

Figure 4. Schematic of the experimental setup for attosecond streaking experiments on nanoparticles. A beam of isolated nanoparticles is illuminated with few-cycle NIR and XUV pulses along the *y*-axis. The inset shows the transmission electron micrograph of the SiO_2 nanoparticles with a diameter of 50 nm. The XUV and NIR pulses propagate in positive direction along the *x*-axis, and are polarized along the *y*-axis. The electron emission is projected with a static electric field onto the MCP/phosphor screen assembly of the VMI spectrometer and each shot is detected with a fast CMOS-camera outside of the vacuum chamber (not shown).

nozzle. We used the design reported in [49, 50], which has also been successfully employed in photoemission studies from isolated nanoparticles in intense few-cycle fields [51–54]. The initial orifice determines the gas flow through the lens system and reduces pressure from atmosphere to the value required for aerodynamic focusing. In the current setup an orifice of 130 μm is installed. The gas flow is converged and diverged through the focusing lenses which include five apertures (schematically shown in figure 4). With given particle size and gas flow properties, the nanoparticles can efficiently be separated from the carrier gas due to their inertia [55, 56]. The nanoparticles are focused into a tight particle beam after the acceleration nozzle, while the carrier gas is injected effusively, and therefore efficiently removed after some distance from the last aperture of the aerodynamic lens. Three stages of differential pumping system behind the lens

system maintain the pressure in the experimental chamber below 2×10^{-7} mbar with operating nanoparticle source.

The nanoparticle density in the interaction region is limited by multiple factors: (i) the nanoparticle density in the dispersion, (ii) the aerosol generation step where evaporation conditions have to be met to avoid cluster formation, (iii) the aerosol transport system including liquid reflow, drying stage(s), and pressure equalization, (iv) impactor(s) to reduce the amount of clusters in the beam, (v) restrictions of the aerodynamic lens system, including aperture sizes and nanoparticle-size dependent throughput, and finally (vi) the distance from the last aperture to the interaction region. The use of nanoparticle dispersions with small size distributions (below 10%) makes it unnecessary to use differential mobility analysis, increasing the nanoparticle density in the interaction region. In experiments on SiO_2, the 50 nm diameter particles
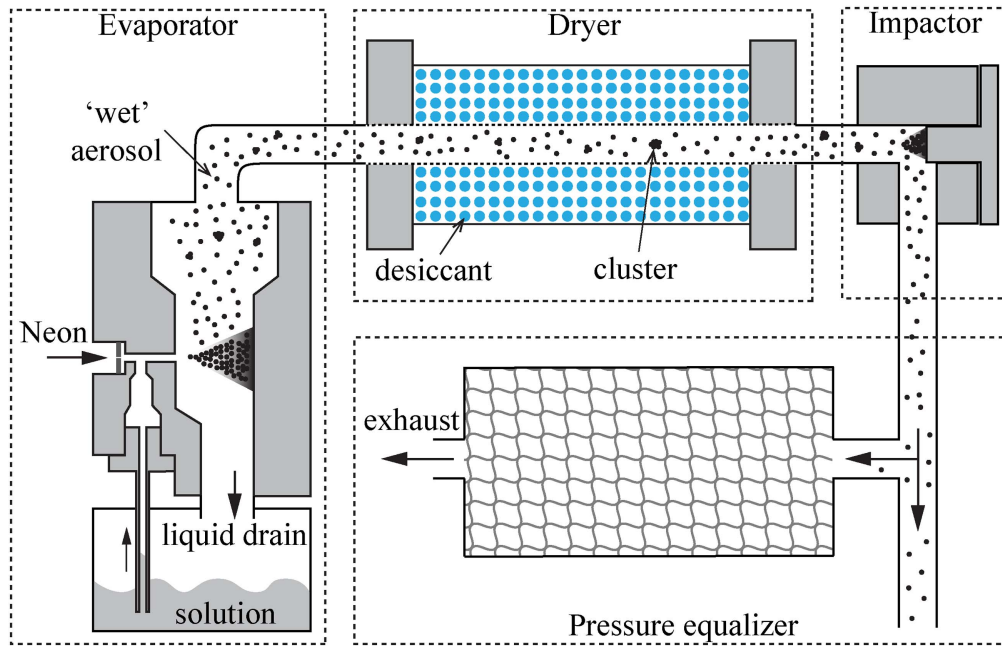
Figure 5. Schematic of the aerosol generation system. The system consisted of an evaporator, silica drying stage, impactor, pressure equalizer, and the aerodynamic lens (not shown).

were prepared by wet chemistry methods based on the Stöber procedure and a seeded growth process [57]. The inset of figure 4 shows the transmission electron micrograph of the SiO_2 nanoparticles with a diameter of 50 nm. The polydispersity of the particles was about 8%.

2.4. Single-shot data discrimination

A distinct advantage of the single shot detection is the ability to record attosecond photoemission from aerosolized nano-targets and residual gas at the very same experimental conditions. The gas thereby provides a temporal ruler, which permits relative attosecond streaking delay measurements, even under conditions, where the resulting electron momenta overlap. The single-shot data discrimination is related to recent coincidence experiments, where the attosecond streaking from two different gases could be simultaneously measured and distinguished in the data analysis [14]. Without such approaches, either the emission bands have to be spectrally well separated (see e.g. [13, 58]), or measurements have to be taken consecutively, which is, however, difficult due to typically limited long-term interferometer stability. The latter would pose a severe problem for measurements on dilute targets, where acquisition times are long (typically in the range of 45–60 min at 1 kHz for one streaking measurement on nanoparticles).

Due to the magnification setting of the imaging lens, a single electron hit on the MCP/phosphor assembly can illuminate several pixels on the CMOS chip. For sufficiently low density of hits on the detector per laser shot, a centroiding algorithm can be used to uncover the number of electrons recorded in single-shot images [45]. Examples for post-processed single-shot images of the 2D electron momenta (*x* and *y* components), as obtained from the residual gas only and for
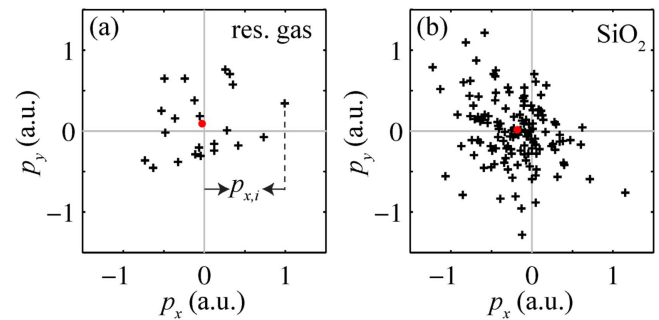
Figure 6. Post-processed single-shot momentum images (projected along p_z) of the electron emission for (a) residual gas and (b) SiO_2 nanoparticles obtained in the XUV-NIR streaking experiments. The red dots show averages of the momentum distributions. The asymmetry in the photoelectron momentum distribution along the laser propagation direction (p_x) originates from preferential absorption of XUV light on the front side of the nanoparticle (shadowing).

SiO_2 nanoparticles, are shown in figures 6(a) and (b), respectively. Note that this analysis differs from the analysis shown in [41], where the centroiding method was not applied.

The laser pulses propagated along the p_x axis, and were polarized along the p_y axis. The number of electrons emitted per laser shot from nanoparticles (figure 6(b)) was typically much larger than from the residual gas (figure 6(a)). For the residual gas frames, single ionization by the XUV is expected to dominate, and the detected electrons therefore originate predominantly from different gas atoms or molecules present in the interaction region. For nanoparticles hit by the XUV, typically more electrons are emitted and show an asymmetry along the laser propagation direction, as depicted in figure 6(b). The asymmetry manifests as more electrons appearing on the left side of the image, corresponding to the incident side along the laser propagation axis. This effect is
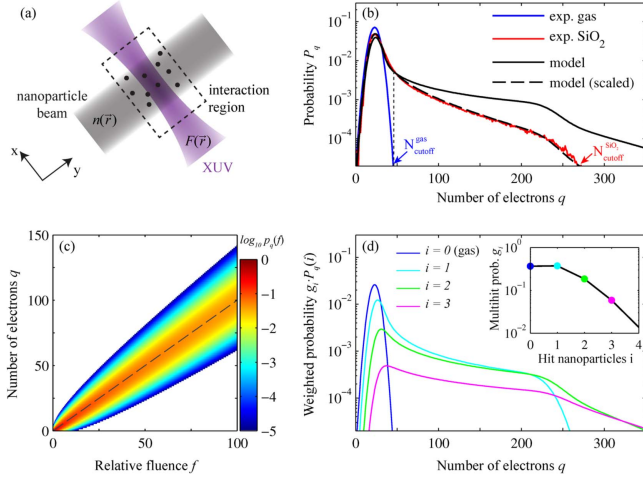
Figure 7. (a) Schematic representation of the XUV and nanoparticle interaction region and the control volume V (dashed rectangle) including N_V nanoparticles. (b) Probabilities to detect q electrons measured from gas (blue) and nanoparticle-gas mixture (red), and calculated from the hit statistics model (solid black). Here, the photoelectron detection probability was $\eta = 8.5\%$. The dashed curve reflects the calculation result scaled with an exponential damping $\exp(q/q_{sat})$, with parameter $q_{sat} = 100$. (c) Single-particle probability distribution $p_q(f)$ in dependence of relative fluence. (d) Weighted multihit probability distributions $g_i P_q^{(i)}$ for hitting $i = 0...3$ nanoparticles. Note that the blue curve ($i = 0$) reflects the gas result. The inset shows the respective multihit probabilities g_i.

known as shadowing [29, 50, 59], and originates from the asymmetric absorption of the attosecond XUV light in the nanoparticle.

In figure 7(b), we plot the histogram of detected electrons per shot for nanoparticles (red line), compared to just residual gas (blue line). Both measurements were performed under identical conditions (laser intensity and experimental chamber pressure ($< 2 \times 10^{-7}$ mbar)), by using the evaporator with just ethanol and with a nanoparticle-ethanol dispersion. Without nanoparticles, the number of electrons per shot has a sharp upper cutoff $N_{cutoff}^{Gas} = 50$. For the nanoparticle dispersion, the maximum number of electrons per shot goes up to $N_{cutoff}^{SiO_2} = 270$, and 15% of the shots recorded more than 50 electrons, which clearly arise from emission from SiO_2 particles.

For the typically employed low nanoparticle densities, on average, less than one nanoparticle is present in the central, high density region of the laser focus. Therefore, even when using the nanoparticle dispersion, the frames contain a signal from residual injection gas and possibly one or a few nanoparticles. In order to quantify the effects of the nanoparticle density, nanoparticle beam parameters and the focal laser intensity profile on the single-shot electron number distribution, we introduce a simplified hit statistics model that is based on the schematic setup shown in figure 7(a). The number density of SiO_2 nanoparticles in the beam is modeled by a Gaussian distribution

$$n(\mathbf{r}) = n_0 \exp(-2(x^2 + z^2)/\omega_{np}^2), \qquad (1)$$

where $n_0 = 1 \times 10^6$ cm^{-3} is the density in the center of the nanoparticle beam and $\omega_{np} = 500$ μm characterizes the beam

width [49]. The XUV fluence (number of photons per unit area) in the focus region is described by a Gaussian beam as

$$F(\mathbf{r}) = \frac{2N_{phot}}{\pi \omega_{XUV}(x)^2} \exp(-2(y^2 + z^2)/\omega_{xuv}(x)^2), \qquad (2)$$

with $\omega_{XUV}(x) = \omega_0 \sqrt{1 + (x/x_R)^2}$ the beam width at position x on the optical axis, $\omega_0 = 10$ μm the beam waist at focus, and $x_R = 8$ mm the Rayleigh length. The total number of photons in a single laser shot was $N_{phot} = 2 \times 10^8$. We now assume that every photon falling into the geometrical cross section $\sigma_{geo} = \pi R^2$ of a nanoparticle with radius $R = 25$ nm is absorbed and generates a photoelectron. This assumption is well justified considering the corresponding attenuation length for the XUV radiation. Considering that each photoelectron is detected with probability η, we can introduce a reference fluence

$$F_{single} = \frac{1}{\eta \sigma_{geo}} \qquad (3)$$

that specifies the fluence needed to generate on average one detected electron per nanoparticle. As a result, the absolute fluence F can conveniently be expressed as a relative fluence $f = F/F_{single}$ that specifies the on average expected measurable electron number per nanoparticle.

In the next step, a simplified rate equation model is employed to describe the probability p_q for measuring q electrons at a given relative fluence. Departing from the initial condition $p_q = \delta_{q,0}$ for a vanishing fluence, the corresponding probability distribution $p_q(f)$ follows from integrating the coupled rate equations

$$\frac{dp_0}{df} = -p_0 \text{ and} \qquad (4)$$

$$\frac{dp_q}{df} = p_{q-1} - p_q \text{ for q} > 0, \qquad (5)$$

as illustrated in figure 7(c). Integrating over a sufficiently large control volume V, which can be chosen to contain an integer number $N_V = \int n(\mathbf{r})$ of nanoparticles yields the probability distribution $P_q = \int p_q(f(\mathbf{r})) d^3r$ for measuring a specific electron number q from a nanoparticle. Note that the distribution P_q so far reflects only the result for a single nanoparticle and is normalized automatically to $\sum_{q=0}^{\infty} P_q = 1$. The probability to hit a selected specific nanoparticle in the control volume is $P_{hit} = \sum_{q=1}^{\infty} P_q$.

Based on this individual hit probability and using a known number of nanoparticles N_V in the control volume, we can introduce the multihit probability to simultaneously hit i nanoparticles as

$$g_i = \binom{N_V}{i} (P_{hit})^i (1 - P_{hit})^{N_V - i}. \qquad (6)$$

The resulting multihit probabilities for the given parameters and for $i = 0...3$ are displayed in the inset of figure 7(d). Note that for the case of $i = 0$, only the residual gas signal is considered. Starting from the corresponding electron number distribution for residual gas $P_q^{(0)}$, which can be taken from the experiment, the electron number distribution for a given

number of simultaneously hit particles i follows as

$$P_q^{(i)} = \sum_k \sum_l P_k^{(i-1)} P_l \delta_{q,k+l} \text{ for } i > 0. \tag{7}$$

The finally measurable electron number distribution results from the weighted sum of the individual multihit distributions via $P_q^{\text{tot}} = \sum_i g_i P_q^{(i)}$. Figure 7(d) shows the relevant terms $g_i P_q^i (i = 1...3)$ from this simulation and the final result is compared to the experiment in figure 7(b).

The simulated electron number distribution shows similar features to the experimental data, i.e. the pronounced residual gas peak and a plateau-like feature up to high electron numbers. However, the slope of the distribution in the plateau region is steeper in the experiment. Scaling the calculated results with an exponential damping function (dashed curve in figure 7(d)) can reproduce the experimental data. While the origin of such scaling effects in the experiment is unclear, we like to point out that the model has neglected contributions, such as shot to shot fluctuations of the XUV pulse energy, quenched electron emission resulting from Coulomb blockade effects or saturation in the electron detection.

In order to select the frames that contain photoemitted electrons from SiO$_2$ nanoparticles, we calculate the average momentum component in the propagation direction $\langle p_x \rangle = \frac{1}{N}\sum_{i=1}^N p_{x,i}$ to quantify the asymmetry in the electron emission. Here, N is the number of electrons per shot, and $p_{x,i}$ is the x-component of the momentum of the i-th detected electron as illustrated in figure 6(a). The single frame distributions as a function of $\langle p_x \rangle$ and the number of electrons per frame are presented in figure 8(a) for a measurement with nanoparticles injected in the interaction region. The black solid line indicates the weighted average of $\langle p_x \rangle$ of the frames with different numbers of electrons. The frames below the blue line (36 electrons) contain less electrons symmetrically distributed, and are assigned to residual-gas-only frames. This can be verified by an independent residual-gas-only measurement with similar laser conditions, as shown in figure 8(b). The residual-gas-only frames contain less than 30 electrons and the average momentum distribution is symmetric with respect to the laser propagation direction.

Due to the limited number of electrons in each frame, the average projected momentum, $\langle p_x \rangle$ of the residual-gas-only frames shows a relatively wide distribution. A significant number of frames above the red line (70 electrons) contain larger amount of electrons and an asymmetric distribution due to the photoemission from nanoparticles (see also figure 6(b)). The frames with hit numbers in between the blue and red lines barely contain electrons from nanoparticles and are disregarded. The discussed features of the nanoparticle frames, i.e. the combination of the number of electrons and an asymmetric distribution, provide an efficient discrimination method for the post-selection of residual-gas-only and nanoparticle frames. The shot-averaged images following this approach are shown in figures 8(c) and (d). The residual gas momentum distribution is symmetric with respect to the laser propagation direction (figure 8(d)), while the nanoparticle emission clearly has an asymmetric distribution due to the XUV shadowing, see figure 8(c).
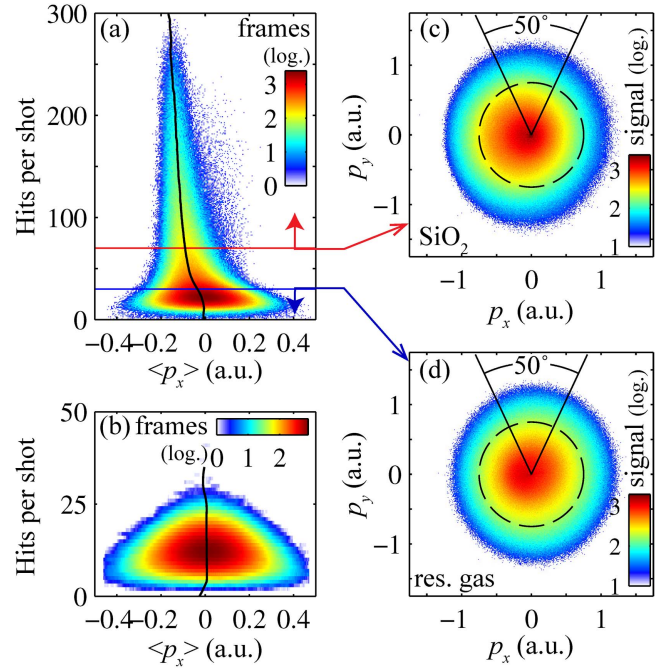

Figure 8. Single frame distributions as a function of $\langle p_x \rangle$ (average projected momentum on the x-axis) and the number of electrons per frame for measurements with (a) SiO$_2$ nanoparticles and (b) without nanoparticles, corresponding to just residual gas. The color scale corresponds to the number of frames on a logarithmic scale. The black solid line indicates the weighted average of $\langle p_x \rangle$. The blue and red solid lines denote regions for nanoparticle and residual-gas-only frames. (c), (d) Images obtained by superposition of nanoparticle frames (above the red line in (a)) and residual-gas-only frames (below the blue line in (a)). The black lines mark the integration range used for retrieving streaking traces.

2.5. Analysis of nanoparticle streaking spectrograms

By measuring momentum images for different pulse delays of the NIR with respect to the XUV pulse, streaking spectrograms can be obtained. In the measurements on 50 nm SiO$_2$ particles, the pulse delay step size was set to 150 as, and 40 000 laser shots were recorded at each delay step. The spectrograms depicted in figure 9 were derived from angular integration of the projected momentum distributions over an angular range of $\pm 25°$ around the laser polarization direction (see figure 8(c) and (d)). We note here that the VMI images were not inverted and the spectrogram was directly obtained from converting the projected radial momenta to energies. This needs to be taken into account when comparing the data to theoretical simulations. Figure 9 shows streaking spectrograms for (a) residual gas and (b) nanoparticles, obtained from the discriminated single-shot data. Both spectrograms look very similar and exhibit the characteristic oscillations with respect to the pulse delays. Two contour lines for a selected asymptotic energy (25 eV) are shown as solid cyan lines.

To determine relative streaking delays between the nanoparticle and residual-gas data, we fit contour lines in the streaking spectrograms. Furthermore, each contour line was filtered to remove high frequency noise (circles in figures 10(a) and (b)) by employing a low-pass filtering. The filtered contour
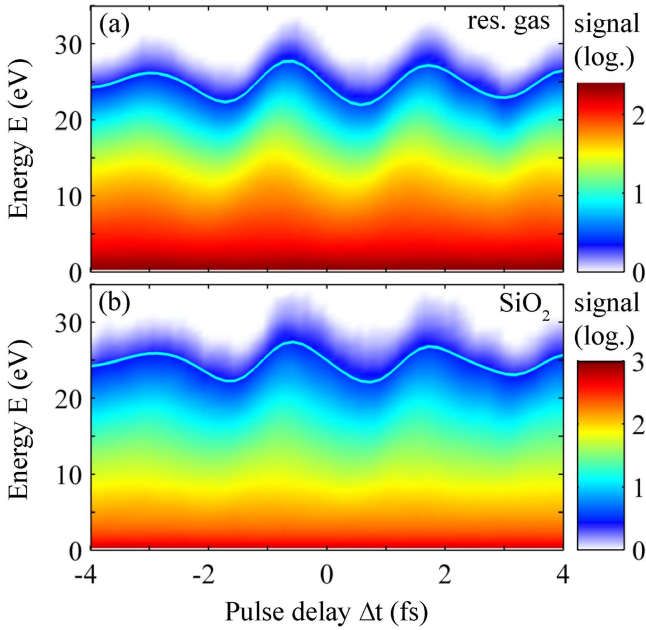
Figure 9. Typical streaking spectrograms of electrons emitted from residual gas (a) and nanoparticles (b) obtained from angular integration of projected momentum maps over ±25° around the laser polarization direction. The solid curves indicate the filtered contour line following constant signal intensity for an asymptotic energy of 25 eV.

lines were then fit with a few-cycle waveform of the following form:

$$E_{\mathrm{fit}}(\Delta t) = E + A \cos\left(\omega \Delta t - \omega \delta t\right) \exp\left(-\frac{1}{2}\frac{(\Delta t - t_0)^2}{\tau^2}\right),$$

where E is the asymptotic energy of the considered contour line, A is the streaking amplitude, ω is the carrier angular frequency, δt is the streaking delay, t_0 is the center of the Gaussian envelope, and τ is the pulse width. The solid lines in figures 10(a) and (b) show the fitting results corresponding to the filtered contour lines in figures 9(a) and (b), respectively. Both curves provide a very good representation of the data and reveal a relative time shift between the curves from the residual gas and SiO_2 nanoparticle. Meanwhile, an effective electric field amplitude of the streaking NIR laser pulse can be reconstructed from the fitted curve for the residual gas. The maximum electric field is $E_y = 2.6 \times 10^9$ V m^{-1}, corresponding to an instantaneous intensity of 9.0×10^{11} W cm^{-2}.

The energy-dependent temporal streaking delays δt_{gas} for the residual gas and δt_{SiO_2} for SiO_2 nanoparticles are shown with blue and red dots in figure 10(c). Both of the curves exhibit a characteristic tilt originating from the chirp of the XUV pulses, which can be fully taken into account in theoretical simulations (for details, see [41]).

In the single-shot attosecond streaking experiments, the simultaneous measurement of the residual gas and nanoparticles within the same experiment offers retrieving the energy-dependent relative streaking delay $\delta t_{\mathrm{rel}} = \delta t_{SiO_2} - \delta t_{\mathrm{gas}}$, which reveals a photoemission time shift between the gas reference and nanoparticles.

In the data discrimination, we accounted for the fact that the recorded events in nanoparticle frames also contain

contributions from the residual gas. In order to calculate the time delay of the photoelectrons from the nanoparticles, it is crucial to uncover the ratio between these two contributions. For this purpose, we compared the averaged single-frame spectra from figures 8(d) and (c), which correspond to the residual gas and nanoparticle frames, respectively. Figure 11(a) shows the resulting spectrum from residual gas (blue line) and the spectrum obtained from the nanoparticle frames (red line). The black line shows the nanoparticle single frame spectrum after subtracting the gas contribution, reflecting the pure nanoparticle signal. The nanoparticle spectrum has a higher intensity and higher spectral cutoff than the residual gas data. The ratio between the nanoparticle and residual gas signal as function of energy is shown in figure 11(b). The contribution of photoelectrons from the SiO_2 nanoparticles increases above 20 eV, and dominates the signal beyond the cutoff energy of the residual gas. Limited by too strong an overlap between the residual gas and nanoparticle signals below 20 eV and the signal-to-noise ratio of the streaking spectra near the cutoff energies (see figure 9), the relative streaking delay between SiO_2 and the reference gas can be extracted in the window between 20 and 30 eV. We note that this particular energy window was accessible with the XUV pulses generated in Kr. Using other generation gases, the window can be tuned, see figure 2.

3. Discussion

To unravel the physics resulting in the delayed photoemission from the dielectric nanoparticles, semi-classical trajectory simulations based on the mean-field Mie Monte-Carlo (M³C) model were employed [53, 54, 60, 61]. In these simulations, the propagation of the XUV and NIR pulses was evaluated using a spectral decomposition of the incident fields and calculating the spatial modes for the individual spectral components using the Mie-solutions for a sphere including dispersion. Photoelectron trajectories were launched in the sphere via Monte-Carlo sampling of the local instantaneous spectral photoionization rate (calculated from the local XUV near-field) and integrated in the NIR near-field using classical equations of motion. For trajectories inside the sphere, elastic electron–atom and inelastic electron–electron collisions were included as instantaneous, isotropic scattering events using energy-dependent mean-free paths and sampled with Monte-Carlo methods (for details see [41]). As ionization due to the XUV field was weak in the investigated scenario, charge interaction effects could be neglected.

From M³C simulations for the experimental parameters, we calculated streaking spectrograms and extracted energy-dependent streaking delays using the same projections and analysis as for the experimental data. The excellent agreement of simulations and experiment (compare curves and dots in figure 10(c)) motivated a systematic analysis of the contributions to the streaking delays. We found that in our scenario the streaking delay for the SiO_2 nanoparticles $\delta t_{SiO_2} = \delta t_{\mathrm{offset}} + \delta t_{\mathrm{chirp}} + \delta t_{\mathrm{fields}} + \delta t_{\mathrm{coll}}$ includes the following four contributions. First, a delay induced by the
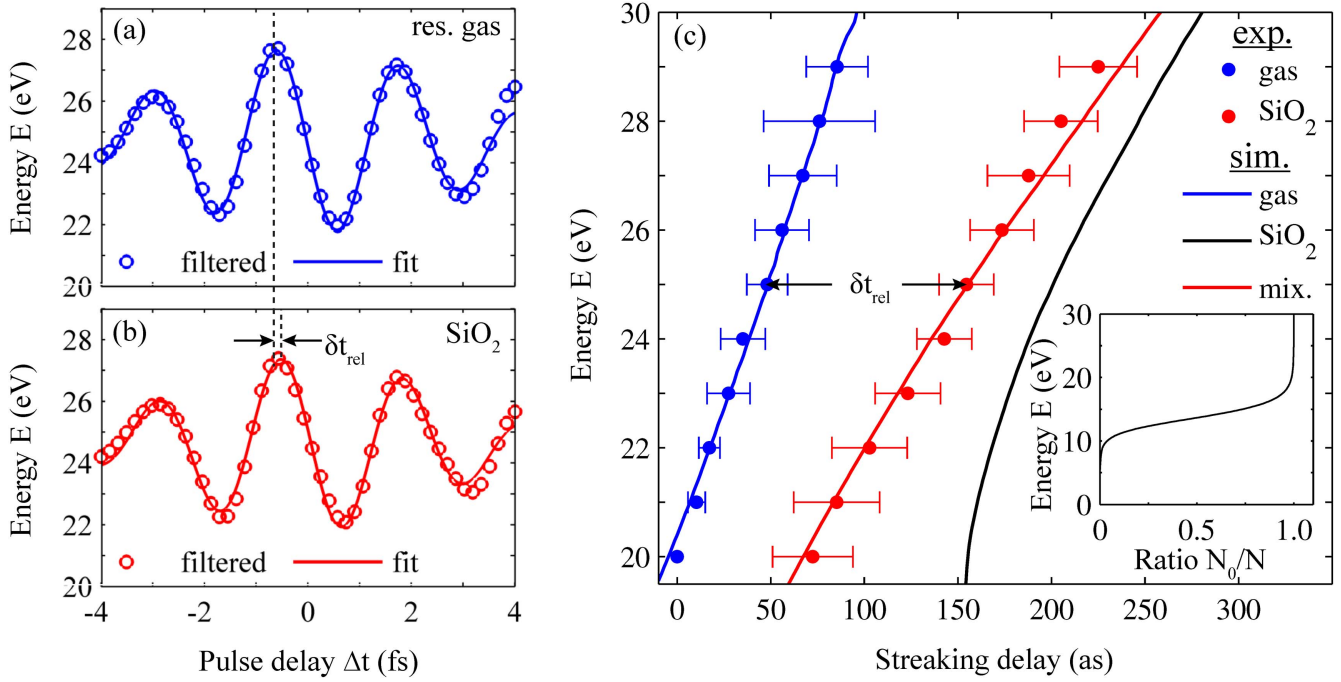
Figure 10. (a), (b) The high frequency-filtered contour lines (circles) were fitted with few-cycle waveforms. (c) Energy-dependent streaking delays measured for residual gas (blue) and SiO_2 nanoparticles (red). The data represents an average over three scans performed under similar conditions (the error bars indicate the deviation of the individual data sets). Solid lines show corresponding simulation results for gas (blue), nanoparticles (black) and their mixture (red) using an XUV chirp of -7×10^{-3} fs^2. The inset shows the relative contribution of electrons without inelastic collisions in the M^{3}C simulations.
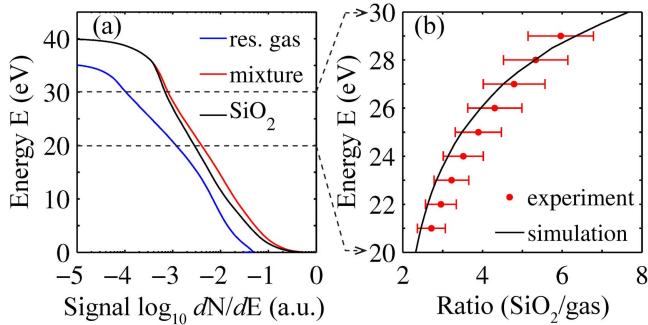

Figure 11. (a) Typical single-frame energy spectra of emitted electrons from residual gas (blue), from a mixture of SiO_2 and residual gas (red), and SiO_2 excluding residual gas (black). (b) Measured energy-dependent ratio of nanoparticle signal relative to residual gas (red) and result obtained from combining simulated gas and nanoparticle spectrograms (black). The error bars indicate the deviation of three independent measurements.

(experimentally unknown) absolute offset of the XUV/NIR delay axis as well as the CEP of the NIR pulse (δt_{offset}). Second, an energy-dependent delay generated by the chirp of the attosecond pulse (δt_{chirp}). Third, a delay induced by the retardation and spatial inhomogeneity of the local near-fields (δt_{fields}, details below) and fourth, a delay induced by the electron collisions inside the medium (δt_{coll}). Since the first two contributions also define the delay of the reference measurement ($\delta t_{gas} = \delta t_{offset} + \delta t_{chirp}$), the relative streaking delay $\delta t_{rel} = \delta t_{SiO_2} - \delta t_{gas} = \delta t_{fields} + \delta t_{coll}$ is fully determined by the field- and collision-induced contributions. The field contributions are relevant for nanoscopic targets such as

the nanoparticles discussed here, but do not play a role in the photoemission from atoms. Note that additional contributions due to Wigner delays [62] and Coulomb-laser coupling [63–65] are assumed to be comparable for nanoparticles and gas as we evaluate similar electron energies and the long-range interactions are Coulombic in both cases. These contributions thus cancel in the relative delay. The remaining short-range effects are assumed negligible away from resonances [66].

In order to extract information on the electron scattering within the material the field-induced contribution to the relative streaking delay must be either negligible or known. In the following we describe how this contribution can be estimated for the example of 50 nm silica spheres. We split the field-induced delay $\delta t_{field} = \delta t_{retard.} + \delta t_{inhom.}$ into the parts corresponding to retardation of the XUV and NIR fields ($\delta t_{retard.}$) and the part reflecting the effect of the spatial inhomogeneities of the NIR field ($\delta t_{inhom.}$), i.e. its decay with increasing distance from the nanosphere.

The retardation effect can be estimated by comparing the evolution of the local near-fields at the sphere surface (in the $z = 0$ plane, see figure 12(a)) with respective vacuum solutions. The XUV field enters the dynamics only via photoionization, which is determined by the pulse envelope. Therefore, we evaluate the group delay $t_{group,XUV} = t_{group,XUV}^{SiO_2} - t_{group,XUV}^{vac}$, defined via the center of mass of the field envelope (blue curve in figure 12(c)), where a negative/positive delay indicates advanced/retarded arrival of the near-field with respect to the vacuum case. For the NIR field,
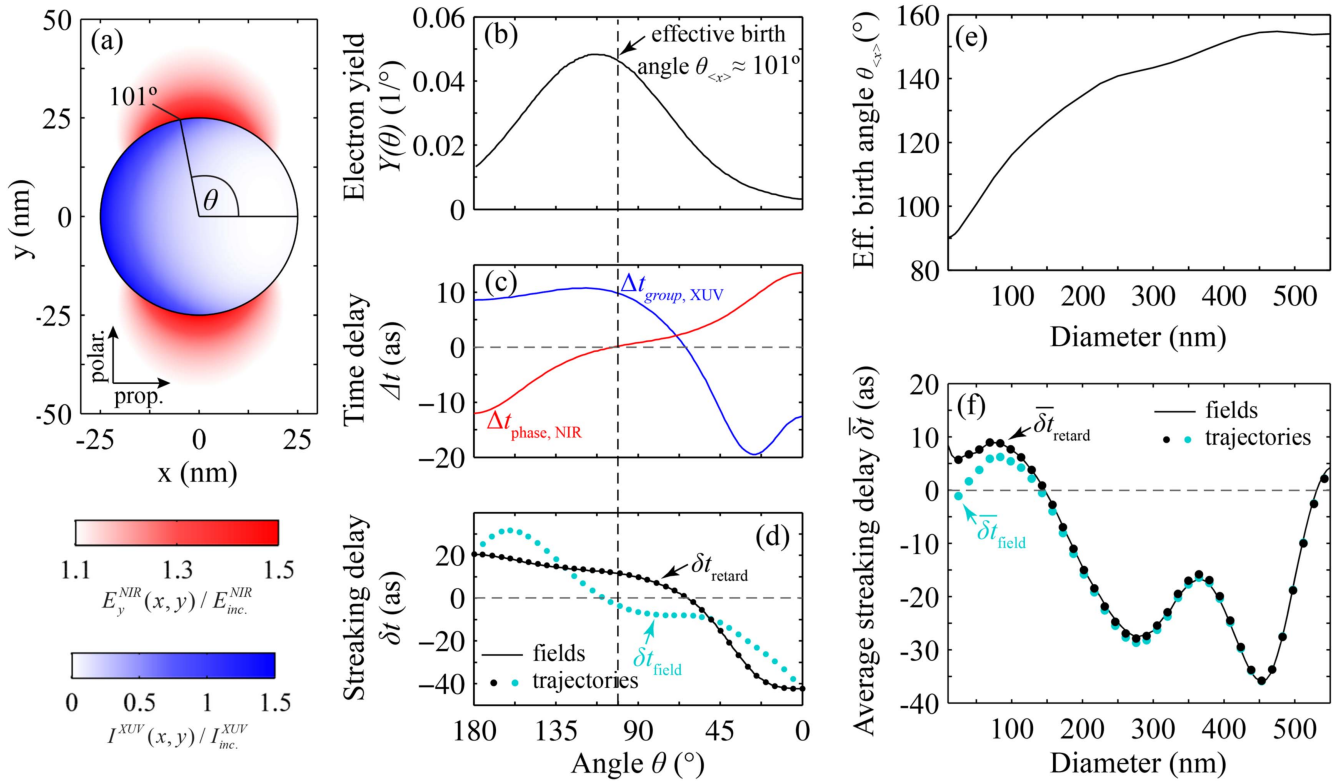
Figure 12. (a) Near-field enhancement of the XUV (blue) and NIR (fields) on a cut through the propagation-polarization plane of a 50 nm SiO$_2$ sphere. (b) Distribution of emitted electrons, $Y(\theta)$, as a function of birth angle θ. The vertical dashed line indicates an effective birth angle $\theta_{\langle x \rangle} = \mathrm{acos}\big(\langle \cos\theta \rangle\big)$. (c) Angle-dependent NIR phase- and XUV group-delay with respect to the vacuum solutions calculated at the sphere surface in the propagation-polarization-plane. (d) Streaking-delay due to field retardation of XUV and NIR fields calculated from the group and phase delays in (c) (black curve). Symbols show streaking delays evaluated from a simplified trajectory model (see text) including only field retardation (black), and including both field retardation and NIR field inhomogeneity (cyan). (e) Evolution of the effective birth angle with the nanoparticle diameter. (f) Size-dependence of the angle-averaged streaking delay $\overline{\delta t} = \frac{\int Y(\theta)\delta t(\theta)\mathrm{d}\theta}{\int S(\theta)\mathrm{d}\theta}$ (weighted with the birth angle distribution) calculated from the near-fields (curve) and from the simplified trajectories model (dots) as in (d).

where the full waveform enters the dynamics, we estimate the retardation effect via the phase delay $t_{\mathrm{phase,NIR}} = t_{\mathrm{phase,NIR}}^{\mathrm{SiO_2}} - t_{\mathrm{phase,NIR}}^{\mathrm{vac}}$ (red curve in figure 12(c)). The overall retardation induced streaking delay then reads $\delta t_{\mathrm{retard.}} = t_{\mathrm{group,XUV}} - t_{\mathrm{phase,NIR}}$, where the XUV/NIR parts contribute with positive/negative sign as the incident NIR-field needs to be delayed/advanced to compensate for the respective retardation effect. We found that the retardation induced delay (black curve in figure 12(d)) is smaller than 40 as over the whole surface of the sphere. However, due to the shadowing of the XUV radiation, the dominant part of the detected photoelectrons is emitted from the front side of the sphere (see figure 10(b)). In particular, at the effective birth angle $\theta_{\langle x \rangle} \approx 101°$ (see dashed vertical line in figures 12(b)–(d)), the retardation induced delay is particularly small (<15 as).

To demonstrate that the delay due to field retardation directly enters the streaking delay, we employed the following simplified trajectory model. Trajectories start at the peak of the local XUV field at the surface with initial momenta pointing away from the sphere and are propagated in the NIR surface field, i.e. without including its decay into free space. In this case, the propagation is not influenced by collisions inside or by field inhomogeneities outside of the particle. Therefore, the resulting

streaking delay includes only the retardation effect and resembles the delay extracted directly from the fields (compare black dots to black line in figure 12(d)). The additional impact of the NIR inhomogeneity can be extracted from the simplified trajectory model when sampling the full NIR field along the trajectories. In that case, the streaking delay includes the retardation and the inhomogeneity effects (cyan dots in figure 12(d)).

For a systematic comparison of the different field-induced contributions to the streaking delay, we calculated angle-averaged streaking delays in dependence of the nanosphere diameter, see figure 12(f). The mean birth angles for the investigated sphere diameters, obtained from M^{3}C simulations, are shown in figure 12(e). The oscillation of the field retardation induced streaking delay as function of sphere diameter (black curve and dots in figure 12(f)) is attributed to the successive excitation of higher order modes of the NIR near-field. The offset of the streaking delay of around 10 as in the limit of small spheres is a pure dispersion induced feature of the XUV near field and not a propagation effect. The additional effect of the NIR inhomogeneity (compare green to black dots in figure 12(f)) is negligible for large spheres but strongly modifies the field induced streaking delay for small spheres. In particular, for $d = 50$ nm the inhomogeneity
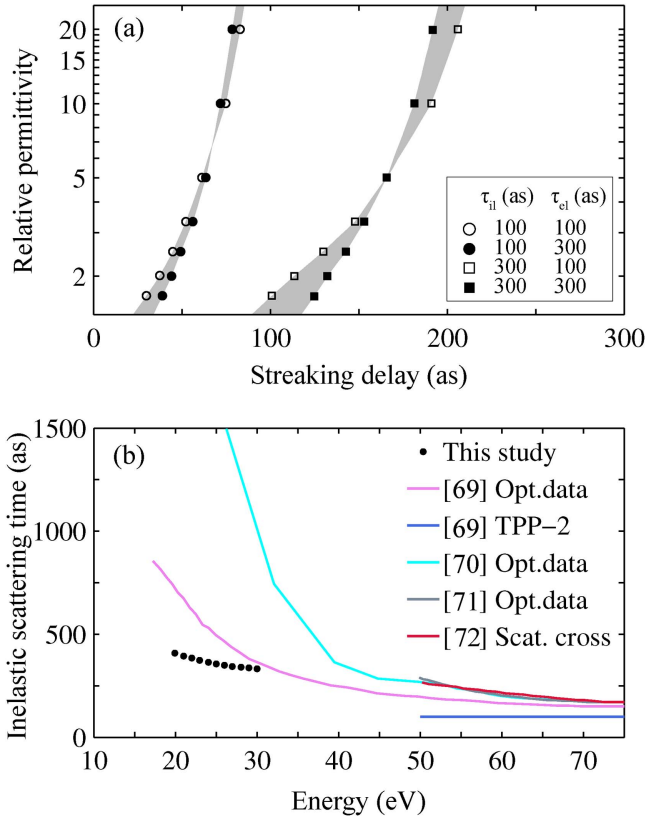
Figure 13. (a) Relative streaking delay in dependence of the materials relative permittivity (for the NIR central wavelength) for different elastic and inelastic scattering times (as indicated). Gray areas visualize the variation when changing the elastic scattering time. (b) Energy-dependent inelastic scattering times measured in our previous study (dots) in comparison with literature data (curves).

Due to experimental and conceptual difficulties in measuring electron inelastic scattering times in solids directly (e.g. by the overlayer method [67]), obtaining information on inelastic electron scattering in solids relied to a large extend on model-based fits of optical transmission and absorption data [68] or simulations, limiting the accuracy of the predictions for electron energies below 50 eV. Figure 13(b)) shows a comparison of the inelastic scattering times obtained via attosecond streaking spectroscopy on SiO_2 nanoparticles in the energy window between 20 and 30 eV to literature values [69–72]. Note that best agreement is found with the work of Tanuma *et al* who state that their data in the range of 10–40 eV is unreliable and only serves as a trend [69]. With inelastic scattering times obtained via attosecond streaking on nanoparticles the predictive capability of theoretical models for scattering in dielectrics can now be thoroughly tested.

4. Conclusions

In conclusion, we have shown that attosecond streaking metrology is a powerful tool for real-time photoemission measurements on isolated nanotargets, and can reveal new insight into e.g. electron scattering. In cases where experiments on solids suffer from accumulative charging, nanoparticle beams provide a solution as a refreshable target. Most importantly, the collective and/or nonlinear dynamics in nanoparticles, such as e.g. localized plasmons [25, 27–30] and plasma waves [73], rapid inner and outer ionization [74], and electron density fluctuations created by, for example, shock waves [75] are interesting phenomena that await their exploration with sub-femtosecond precision. We expect the outlined approaches for the implementation of attosecond streaking in nanoparticles to contribute to further advances in these directions.

effect cancels the retardation effect ($\overline{\delta t} < 2.5$ as) such that field-induced delays are negligible ($\delta t_{\text{fields}} \ll \delta t_{\text{coll}}$), making the relative streaking delay to a direct measure of the collisional delay ($\delta t_{\text{rel}} \approx \delta t_{\text{coll}}$).

To study the physics behind the collisional delay, we systematically analyzed the impact of different elastic and inelastic scattering times (average times between two scattering events, corresponding to their respective mean-free paths) on the calculated streaking delays, see figure 13(a)). We found that for a broad range of dielectric materials (sampled by scanning the relative permittivity at the NIR wavelength) the collisional streaking delay is almost entirely determined by the inelastic scattering time. Our analysis revealed that the additional effect of the elastic scattering time strongly depends on the materials permittivity. While for low permittivities ($\varepsilon_r < 5$) larger elastic scattering times result in larger streaking delays the opposite trend is found for high permittivities ($\varepsilon_r > 5$). Thus, the effect of the elastic scattering time cancels in the intermediate permittivity region of typical dielectric materials. This result shows that experimentally accessible relative streaking delays serve as direct clock for inelastic scattering times in SiO_2. The approach for clocking inelastic scattering times should be transferable to other dielectrics.

ORCID iDs

L Seiffert ● https://orcid.org/0000-0002-2389-5295
T Fennel ● https://orcid.org/0000-0002-4149-5164
M F Kling ● https://orcid.org/0000-0002-1710-0775

References

[1] Hassan M T *et al* 2016 Optical attosecond pulses and tracking the nonlinear response of bound electrons *Nature* **530** 66–70

[2] Kienberger R *et al* 2004 Atomic transient recorder *Nature* **427** 817–21

[3] Hentschel M, Kienberger R, Spielmann C, Raider G A, Milosevic N, Brabec T, Corkum P, Heinzmann U, Drescher M and Krausz F 2001 Attosecond metrology *Nature* **414** 509–13

[4] Paul P M, Toma E S, Breger P, Mullot G, Augé F, Balcou P, Muller H G and Agostini P 2001 Observation of a train of attosecond pulses from high harmonic generation *Science* **292** 1689–92

[5] Krausz F and Ivanov M 2009 Attosecond physics *Rev. Mod. Phys.* **81** 163–234

[6] Gallmann L, Cirelli C and Keller U 2012 Attosecond science: recent highlights and future trends *Annu. Rev. Phys. Chem.* **63** 447–69

[7] Ramasesha K, Leone S R and Neumark D M 2016 Real-time probing of electron dynamics using attosecond time-resolved spectroscopy *Annu. Rev. Phys. Chem.* **67** 41–63

[8] Ciappina M F *et al* 2017 Attosecond physics at the nanoscale *Rep. Prog. Phys.* **80** 054401

[9] Itatani J, Quere F, Yudin G L, Ivanov M Y, Krausz F and Corkum P B 2002 Attosecond streak camera *Phys. Rev. Lett.* **88** 173903

[10] Kienberger R *et al* 2002 Steering attosecond electron wave packets with light *Science* **297** 1144–8

[11] Thumm U, Lao Q, Bothschafter E, Süßmann F, Kling M F and Kienberger R 2015 *Handbook of Photonics* ed D Andrews (New York: Wiley) pp 537–53

[12] Uiberacker M *et al* 2007 Attosecond real-time observation of electron tunnelling in atoms *Nature* **446** 627–32

[13] Schultze M *et al* 2010 Delay in photoemission *Science* **328** 1658

[14] Cirelli C, Sabbar M, Heuser S, Boge R, Lucchini M, Gallmann L and Keller U 2015 Energy-dependent photoemission time delays of noble gas atoms using coincidence attosecond streaking *IEEE J. Sel. Top. Quantum Electron.* **21** 1–7

[15] Ossiander M *et al* 2017 Attosecond correlation dynamics *Nat. Phys.* **13** 280–5

[16] Cavalieri A L *et al* 2007 Attosecond spectroscopy in condensed matter *Nature* **449** 1029–32

[17] Neppl S, Ernstorfer R, Bothschafter E M, Cavalieri A L, Menzel D, Barth J V, Krausz F, Kienberger R and Feulner P 2012 Attosecond time-resolved photoemission from core and valence states of magnesium *Phys. Rev. Lett.* **109** 087401

[18] Okell W A *et al* 2015 Temporal broadening of attosecond photoelectron wavepackets from solid surfaces *Optica* **2** 383–7

[19] Locher R, Castiglioni L, Lucchini M, Greif M, Gallmann L, Osterwalder J, Hengsberger M and Keller U 2015 Energy-dependent photoemission delays from noble metal surfaces by attosecond interferometry *Optica* **2** 405–10

[20] Borisov A G, Sánchez-Portal D, Kazansky A K and Echenique P M 2013 Resonant and nonresonant processes in attosecond streaking from metals *Phys. Rev.* B **87** 121110

[21] Zhang C-H and Thumm U 2009 Attosecond photoelectron spectroscopy of metal surfaces *Phys. Rev. Lett.* **102** 123601

[22] Neppl S *et al* 2015 Direct observation of electron propagation and dielectric screening on the atomic length scale *Nat. Phys.* **517** 342–6

[23] Liao Q and Thumm U 2015 Attosecond time-resolved streaked photoemission from Mg-covered W(110) surfaces *Phys. Rev.* A **92** 031401

[24] Stockman M I, Kling M F, Kleineberg U and Krausz F 2007 Attosecond nanoplasmonic-field microscope *Nat. Photon.* **1** 539–44

[25] Süßmann F and Kling M F 2011 Attosecond nanoplasmonic streaking of localized fields near metal nanospheres *Phys. Rev.* B **84** 121406

[26] Skopalova E, Lei D Y, Witting T, Arrell C, Frank F, Sonnefraud Y, Maier S A, Tisch J W G and Marangos J P 2011 Numerical simulation of attosecond nanoplasmonic streaking *New J. Phys.* **13** 083003

[27] Borisov A G, Echenique P M and Kazansky A K 2012 Attostreaking with metallic nano-objects *New J. Phys.* **14** 023036

[28] Kelkensberg F, Koenderink A F and Vrakking M J J 2012 Attosecond streaking in a nano-plasmonic field *New J. Phys.* **14** 093034

[29] Prell J S, Borja L J, Neumark D M and Leone S R 2013 Simulation of attosecond-resolved imaging of the plasmon electric field in metallic nanoparticles *Ann. Phys.* **525** 151–61

[30] Li J, Saydanzad E and Thumm U 2016 Retrieving plasmonic near-field information: a quantum-mechanical model for streaking photoelectron spectroscopy of gold nanospheres *Phys. Rev.* A **94** 051401

[31] Maier S 2007 *Plasmonics: Fundamentals and Applications* (New York: Springer)

[32] Hommelhoff P and Kling M 2015 *Attosecond Nanophysics: From Basic Science to Applications* (New York: Wiley)

[33] Gramov D K and Bozhevolnyi S I 2010 Plasmonics beyond the diffraction limit *Nat. Photon.* **4** 83–91

[34] Wimmer L, Herink G, Solli D R, Yalunin S V, Echternkamp K E and Ropers C 2014 Terahertz control of nanotip photoemission *Nat. Phys.* **10** 432–6

[35] Wimmer L, Karnbach O, Herink G and Ropers C 2017 Phase space manipulation of free-electron pulses from metal nanotips using combined terahertz near fields and external biasing *Phys. Rev.* B **95** 165416

[36] Förg B *et al* 2016 Attosecond nanoscale near-field sampling *Nat. Commun.* **7** 11717

[37] Schötz J, Förg B, Förster M, Okell W A, Stockman M I, Krausz F, Hommelhoff P and Kling M F 2017 Reconstruction of nanoscale near fields by attosecond streaking *IEEE J. Sel. Top. Quantum Electron.* **23** 77–87

[38] Mikkelsen A *et al* 2009 Photoemission electron microscopy using extreme ultraviolet attosecond pulse trains *Rev. Sci. Instrum.* **80** 123703

[39] Chew S H *et al* 2012 Time-of-flight-photoelectron emission microscopy on plasmonic structures using attosecond extreme ultraviolet pulses *Appl. Phys. Lett.* **100** 051904

[40] Mårsell E *et al* 2015 Nanoscale imaging of local few-femtosecond near-field dynamics within a single plasmonic nanoantenna *Nano Lett.* **15** 6601–8

[41] Seiffert L *et al* 2017 Attosecond chronoscopy of electron scattering in dielectric nanoparticles *Nat. Phys.* **13** 766–70

[42] Lücking F, Trabattoni A, Anumula S, Sansone G, Calegari F, Nisoli M, Oksenhendler T and Tempea G 2014 *In situ* measurement of nonlinear carrier-envelope phase changes in hollow fiber compression *Opt. Lett.* **39** 2302–5

[43] Sola I J *et al* 2006 Controlling attosecond electron dynamics by phase-stabilized polarization gating *Nat. Phys.* **2** 319–22

[44] Eppink A T J B and Parker D H 1997 Velocity map imaging of ions and electrons using electrostatic lenses: application in photoelectron and photofragment ion imaging of molecular oxygen *Rev. Sci. Instrum.* **68** 3477

[45] Süßmann F *et al* 2011 Single-shot velocity-map imaging of attosecond light-field control at kilohertz rate *Rev. Sci. Instrum.* **82** 093109

[46] Poletto L, Bonora S, Pascolini M and Villoresi P 2004 Instrumentation for analysis and utilization of extreme-

ultraviolet and soft x-ray high-order harmonics *Rev. Sci. Instrum.* **75** 4413–8

[47] Mairesse Y and Quéré F 2005 Frequency-resolved optical gating for complete reconstruction of attosecond bursts *Phys. Rev.* A **71** 011401

[48] Süßmann F and Kling M F 2011 Attosecond nanoplasmonic streaking of localized fields near metal nanospheres *Phys. Rev.* B **84** 121406

[49] Bresch H 2007 Photoionization of free aerosol particles with synchrotron radiation *Photoionisation von Freien Aerosolpartikeln mit Synchrotronstrahlung* (Berlin: Freie Universität)

[50] Wilson K R, Zou S, Shu J, Rühl E, Leone S R, Schatz G C and Ahmed M 2007 Size-dependent angular distributions of low-energy photoelectrons emitted from NaCl nanoparticles *Nano Lett.* **7** 2014–9

[51] Zherebtsov S *et al* 2011 Controlled near-field enhanced electron acceleration from dielectric nanospheres with intense few-cycle laser fields *Nat. Phys.* **7** 656–62

[52] Zherebtsov S *et al* 2012 Carrier-envelope phase-tagged imaging of the controlled electron acceleration from SiO_2 nanospheres in intense few-cycle laser fields *New J. Phys.* **14** 075010

[53] Süßmann F *et al* 2015 Field propagation-induced directionality of carrier-envelope phase-controlled photoemission from nanospheres *Nat. Commun.* **6** 7944

[54] Rupp P *et al* 2017 Quenching of material dependence in few-cycle driven electron acceleration from nanoparticles under many-particle charge interaction *J. Mod. Opt.* **64** 995–1003

[55] Liu P, Ziemann P J, Kittelson D B and McMurry P H 1995 Generating particle beams of controlled dimensions and divergence: I. Theory of particle motion in aerodynamic lenses and nozzle expansions *Aerosol Sci. Technol.* **22** 293–313

[56] Wang X and McMurry P H 2006 A design tool for aerodynamic lens systems *Aerosol Sci. Technol.* **40** 320–34

[57] Stöber W, Fink A and Bohn E 1968 Controlled growth of monodisperse silica spheres in the micron size range *J. Coll. Int. Sci.* **26** 62

[58] Schultze M *et al* 2014 Attosecond band-gap dynamics in silicon *Science* **346** 1348

[59] Signorell R, Goldmann M, Yoder B L, Bodi A, Chasovskikh E, Lang L and Luckhaus D 2016 Nanofocusing, shadowing, and electron mean free path in the photoemission from aerosol droplets *Chem. Phys. Lett.* **658** 1–6

[60] Seiffert L, Süßmann F, Zherebtsov S, Rupp P, Peltz C, Rühl E, Kling M F and Fennel T 2016 Competition of single and double rescattering in the strong-field photoemission from dielectric nanospheres *Appl. Phys.* B **122** 101

[61] Seiffert L, Henning P, Rupp P, Zherebtsov S, Hommelhoff P, Kling M F and Fennel T 2017 Trapping field assisted backscattering in strong-field photoemission from dielectric nanospheres *J. Mod. Opt.* **64** 1096–103

[62] Wigner E P 1955 Lower limit for the energy derivative of the scattering phase shift *Phys. Rev.* **98** 145–7

[63] Smirnova O, Mouritzen A S, Patchkovskii S and Ivanov M Y 2007 Coulomb-laser coupling in laser-assisted photoionization and molecular tomography *J. Phys. B: At. Mol. Opt. Phys.* **40** F197

[64] Zhang C H and Thumm U 2010 Electron–ion interaction effects in attosecond time-resolved photoelectron spectra *Phys. Rev.* A **82** 043405

[65] Nagele S, Pazourek R, Feist J, Doblhoff-Dier K, Lemell C, Tőkési K and Burgdörfer J 2011 Time-resolved photoemission by attosecond streaking: extraction of time information *J. Phys. B: At. Mol. Opt. Phys.* **44** 081001

[66] Dahlström J M, Guénot D, Klünder K, Gisselbrecht M, Mauritsson J, L'Huillier A, Maquet A and Taïeb R 2013 Theory of attosecond delays in laser-assisted photoionization *Chem. Phys.* **414** 53–64

[67] Palmberg P W and Rhodin T N 1968 Auger electron spectroscopy of fcc metal surfaces *J. Appl. Phys.* **39** 2425–32

[68] Lynch D W, Hunter W R and Palik E D 1985 *Handbook of Optical Constants of Solids* (Orlando, FL: Academic)

[69] Tanuma S, Powell C J and Penn D R 1991 Calculations of electron inelastic mean free paths: III. Data for 15 inorganic compounds over the 50–2000 eV range *Surf. Interface Anal.* **17** 927–39

[70] Ashley J C and Anderson V E 1981 Interaction of low-energy electrons with silicon dioxide *J. Electron Spectrosc. Relat. Phenom.* **4** 127–48

[71] Akkerman A, Boutboul T, Breskin A, Chechik R, Gibrekhterman A and Lifshitz Y 1996 Inelastic electron interactions in the energy range 50–10 keV in insulators: alkali halides and metal oxides *Phys. Status Solidi* b **198** 769–84

[72] Siddharth H P, Vaishnav B G and Joshipura K N 2012 Electron inelastic mean free paths in solids: a theoretical approach *Chin. Phys.* B **21** 093402

[73] Varin C, Peltz C, Brabec T and Fennel T 2012 Attosecond plasma wave dynamics in laser-driven cluster nanoplasmas *Phys. Rev. Lett.* **108** 175007

[74] Georgescu I, Saalmann U and Rost J M 2007 Attosecond resolved charging of ions in a rare-gas cluster *Phys. Rev. Lett.* **99** 183002

[75] Hickstein D D *et al* 2012 Direct visualization of laser-driven electron multiple scattering and tunneling distance in strong-field ionization *Phys. Rev. Lett.* **109** 073004